The International Journal of Advanced Manufacturing Technology (2024) 130:3917–3928
https://doi.org/10.1007/s00170-023-12901-0

ORIGINAL ARTICLE

Effects of particle damper design parameters on the damping performance of laser powder bed fused structures

Birol Ozcevik[1,2] · Emrecan Soylemez[1] · Bekir Bediz[3] · Ugur Simsek[2]

Received: 30 May 2023 / Accepted: 23 December 2023 / Published online: 10 January 2024

Abstract

Particle dampers (PD), a passive damping technology, absorb energy from particle-particle and particle-cell wall interactions originating from friction and collision. PDs offer advantages such as design simplicity, low cost, applicability in harsh conditions, and flexibility to be used in a wide frequency band range. Additive manufacturing, specifically the powder bed fusion process, can fabricate structures with integrated PDs in a single printing process, eliminating the need to implement external dampers. However, the dynamic behavior of PDs must be determined to utilize their full potential. In this study, we examined 16 cases of integrated PDs by varying specific parameters including size, number, and locations on the structure to understand the effects of these parameters on the dynamic behavior of the first and second modes of the structure. Modal tests were conducted on additively manufactured samples to extract frequency response functions and calculate modal parameters (natural frequency and damping ratio) using the rational fraction polynomial method, studying the effects of PDs. The results showed that the damping performance of the parts was increased by a factor of up to 10 using body-integrated PDs compared with the fully fused specimen. The effectiveness of body-integrated PDs was shown to be strongly dependent on their volume and location. For instance, the damping generally increased as the volume fraction increased, which also reduced the total weight of the specimens by up to 60 g. Furthermore, the damping performance significantly increased for a specific mode when the PDs were located near the maximum displacement regions.

Keywords Particle damping · Additive manufacturing (AM) · Laser powder bed fusion (L-PBF) · Inconel 718 · Dynamic behavior · Damping ratio

1 Introduction

Particle dampers (PD) offer numerous benefits compared with conventional damping methods, such as simplicity in design, low cost [1–4], long component life [1], superior performance at high temperatures and oil-contaminated conditions [2, 5–8], and broadband damping [9–13]. Owing to these advantages, PDs are used in numerous industries, including medical, energy, automotive, and aerospace [14]. The damping performance of PDs can be tailored by exploiting the complex design freedom/benefits of additive manufacturing (AM) [9]. Huang et al. highlighted that AM made it more feasible to produce complex geometries without relying on the principles of assembly or traditional manufacturing methods [15] which is important to manufacture PD-integrated bodies without taking into account the limitations of traditional manufacturing methods. Pereira et al. also pointed out that while emphasizing the efficiency of AM due to its capacity for large-scale production, its advantages in terms of customization and the creation of complex designs allow it to outperform traditional manufacturing methods [16] that demonstrates the utility of AM, particularly in specialized designs such as PD-integrated structures. With considering these advantages, as AM process laser powder bed fusion (L-PBF) is preferred for PD functional integration because the powder particles inside the cavities are not sintered during fabrication, as opposed to electron beam melting or binder jetting processes [9].

✉ Emrecan Soylemez
esoylemez@itu.edu.tr

[1] Department of Mechanical Engineering, Istanbul Technical University, Gumussuyu, Beyoglu, Istanbul 34437, Türkiye

[2] Engineering Department, GE Aerospace, Gebze, Kocaeli 41471, Türkiye

[3] Mechatronics Engineering Program, Faculty of Engineering and Natural Sciences, Sabanci University, Tuzla, Istanbul 34956, Türkiye

Furthermore, L-PBF offers design flexibility by allowing the adjustment of the geometry [9] and location [17] of unfused powder. This flexibility allows topology-optimized low-weight structures with low-vibration amplitudes for various applications of PDs including automobiles, machine tools, helicopter blades, and wind turbines [18]. The introduction of L-PBF was a milestone in the development of these applications; however, the effects of PDs on the dynamic behavior of these structures must be fully understood to maximize their potential [19, 20].

One approach to examining the dynamic behavior of PDs is numerical modeling. Considering their nonlinearity, however, predicting their effects on the dynamic behavior of the fabricated parts is challenging. Pourtavakoli et al. claim that the discrete element method (DEM) is one of the preferred computational approaches for analyzing the dynamics of PDs by employing unit cells of particle regions [21]. However, DEM is computationally intensive because unfused cavities necessitate the analysis of millions of particles [22]. Saeki applied the multi-unit PD method, which involves the linear superposition of one unit cell [5]. Despite this, particle-based numerical simulations using DEM are not able to evaluate the design parameters that have the most significant impacts on damping, such as excitation level, cavity dimensions, or packing density [4, 6]. Harduf et al. proposed an effective and computationally efficient two-mass model that distinguishes between the powder and fused volume [23]. The study explained and demonstrated the sliding friction and inertial effects of particles on the damping ratio. It concluded that large excitation levels make the friction effect insignificant [23]. However, for a more comprehensive understanding of parameter effects and validation, experiments need to be conducted.

Ehlers et al. experimentally evaluated the influence of design parameters, such as excitation level, particle mass, packing density, and PD (cavity) dimensions, on the dynamics of fabricated parts with PDs [9, 24]. The effects of PDs on Al-Si-10Mg unconstrained beams fabricated using L-PBF were investigated by impulse hammer excitation which was controlled using a motor [9]. A significant decrease in vibrational amplitude was observed using PDs while achieving broadband damping from the first to the seventh bending mode [9]. It was also shown that the damping behavior depends on the frequency and can be increased by a factor of 20. Furthermore, Ehlers et al. studied the sensitivity of damping to the excitation of the force amplitude (i.e., the deformation amplitudes of the parts) and concluded that the extracted damping ratios do not change significantly for impact force magnitudes above 100 N [9]. However, for lower impact force magnitudes, damping increases as the magnitude of the force increases because the particles must initially overcome stiction [10]. Scott-Emuakpor et al. and Goldin et al. also investigated the effect of PD position and the number of PDs on L-PBF-manufactured Inconel 718 (IN718) and AISI 316L beams [17, 25–29]. Modal tests were conducted using a shaker to evaluate the damping capability in four different beam configurations under clamped-free boundary conditions. The four configurations with internal unfused powder volumes of 1–4% showed up to 10-fold increases in damping compared with the fully fused solid beams for the first three bending modes [17, 26].

The researchers warn that cavity volume fraction above the 1–4% range would be detrimental to structural integrity [26]. Determining the threshold of the volume fraction is crucial for producing parts that are mechanically similar to the fully dense versions but with optimal damping performance [26]. In a recent study, a compressor-like blade geometry was employed to determine the unfused powder volume effective threshold [27]. This study confirmed that the unfused cavities can be utilized to suppress the vibrations in complex structures, even when the total unfused volume is less than 1%. Furthermore, the damping performance of PDs becomes stable after millions of cycles applied at high strain ranges; although a substantial drop in the damping performance of the beam with PDs is observed, it is still two times higher than that of a fully dense version [27].

The impacts of key design parameters, including cavity location, cavity number, and cavity dimension, have been individually investigated, but no optimization study has comparatively quantified the influence of multiple design parameters on damping performance. Additionally, there is no study in the literature addressing the design considerations of the PD position and size based on the deformation profile of the mode shapes within the frequency range of interest. Therefore, the goal of the present study is to quantify the combined impacts of the volume of unfused powder, cavity number, and cavity location on particle damping performance. Ultimately, another aim is to correlate these results with the deformation profiles of the mode shapes and demonstrate the connection between the improvement in position and size of PD with mode shape. To accomplish this, a design of experiments (DoE) approach is taken considering these design parameters that includes 16 samples with PDs and a fully fused Inconel 718 beam manufactured by L-PBF. Experimental modal analysis is performed by impulse excitation, and the influence of PDs is examined in each case and compared with the fully fused sample. In addition, to quantitatively describe the vibration behavior of the printed samples over a range of frequencies, the root sum square (RSS) method is used to generate a key performance metric. Moreover, the damping characteristic of the specimens with unfused cavities is correlated with the mode shapes obtained from finite element analysis (FEA). The results show that the damping performance of PD-integrated specimens is 10 times higher than that of a similar component made of fully fused powder. This DoE study may

serve as a benchmark for evaluating the damping behavior of beams with integrated PDs.

2 Materials and methods

2.1 Design of experiments (DoE)

To evaluate the effects of size, location, and number of damper cavities on the damping performance, 16 specimens with integrated PDs were designed and additively manufactured (see Fig. 1). A fully fused specimen was also included as the control specimen. The external dimensions of the specimens are 148 mm × 60 mm × 10 mm, as seen in Fig. 1b. The thickness and width of the PDs are 6 mm and 40 mm, respectively, and centered in both directions, whereas the location of the PDs vary, and the length is 20 mm, 40 mm, and 80 mm.

The specimens were grouped by LEN, LOC, and NOD to determine the effects of the cavity length, location, and number of dampers on the damping performance, respectively, as defined in Table 1. The specimens in the LEN groups were designed to examine the effect of PD length on damping performance. The regions (center or tip) and the number of PDs were designed to isolate one variable in each LEN group. LOC 1–6 were designed to examine the effect of the PD locations for different numbers and sizes of PDs. Finally, NOD 1–4 were designed to examine the effect of the number of PDs. Specifically, NOD 1–2 and NOD 3–4 were designed to investigate the PDs located at the center and the tip of the beam, respectively. Figure 1a depicts the schematic side views of the specimens.

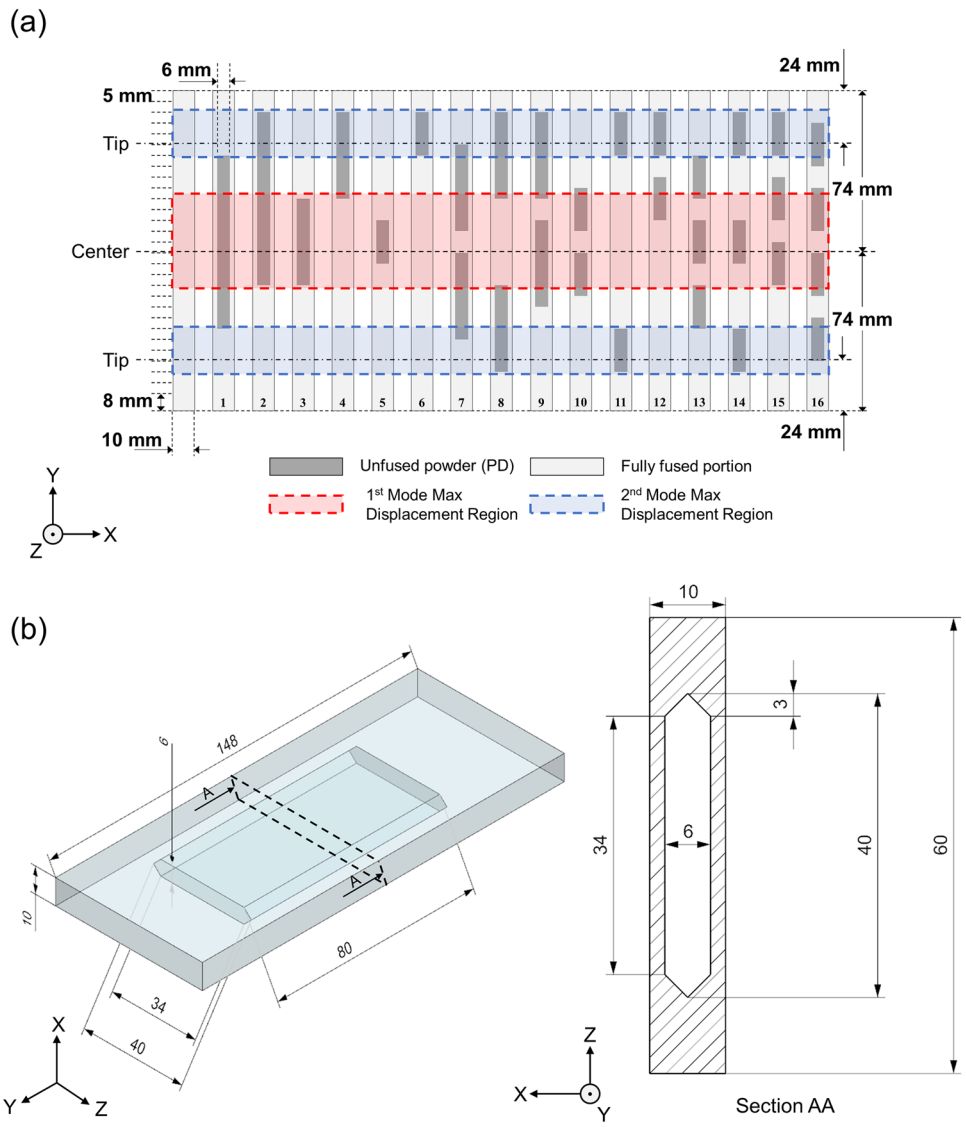

Fig. 1 **a** Schematic side view of specimens. Geometric center and tips of the specimen showed with dashed line. The region of maximum displacement due to the first mode is shown with the red rectangle, and the maximum displacement regions due to the second mode are shown with the blue rectangles. **b** 3D CAD model of specimen 1 and the section view of PD cavities in all specimens

Table 1 Designed specimens in groups according to the investigated parameter

Parameter definition	Group name	Specimens in group
I) Effect of the PD length	LEN 1	1, 3, 5
	LEN 2	2, 4, 6
	LEN 3	8, 11
	LEN 4	9, 12
II) Effect of the PD location	LOC 1	1, 2
	LOC 2	3, 4
	LOC 3	5, 6
	LOC 4	7, 8, 9
	LOC 5	10, 11, 12
	LOC 6	13, 14, 15
III) Effect of the PD number	NOD 1	1, 7, 16
	NOD 2	3, 10
	NOD 3	2, 9
	NOD 4	4, 12

2.2 Laser powder bed fusion of specimens

The first step of the manufacturing process is creating a build layout in a CAD environment. The build layout should comply with the design for AM best practices, including cross-section approximation, tilt angle, wall thickness, and part size [18]. The build layout for the printed specimens is shown in Fig. 3. The build file was converted to machine-readable format (.cls) and imported to a Concept Laser M2 machine loaded with Inconel 718 powders with particle size distributions of $d_{10} = 23$ µm, $d_{50} = 35$ µm, and $d_{90} = 50$ µm, which were acquired from Praxair. Powder morphology was also examined using scanning electron microscopy (SEM) (Philips XL 30 SFEG), as seen in Fig. 2. The preferred material, Inconel 718, exhibits excellent properties in terms of fatigue resistance, creep resistance, wear resistance, and resistance to hot corrosion [30–32]. It has extensive applications in aviation and power plants [32, 33]. The chemical composition of Inconel 718 powder according to vendor data is given in Table 2 [34].

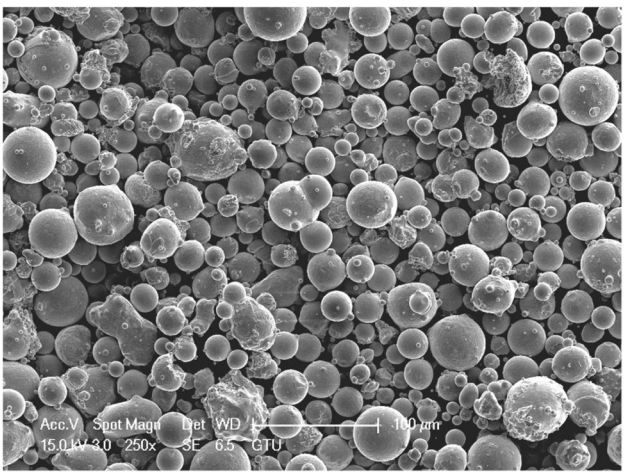

Fig. 2 SEM images of Inconel 718 powder particles at 250 × magnification

Once the print was completed, the powder was evacuated, and the printed specimens were removed from the build plate by wire electrical discharge machining. No heat treatment or surface finishing process was applied to the printed specimens seen in Fig. 3.

Specifying the volume fractions of the PDs is necessary to compare each specimen [9]. In this study, the specimens were weighed using a precision scale (Techfit TF-1010) with 1 g sensitivity. The results are listed in Table 3 along with the volume fraction parameters.

2.3 Numerical modeling

Finite element analysis was performed using ANSYS 19.2 software to determine the natural frequencies (for model validation) and mode shapes (to clarify the effect of PD location and relate the simulations to the experimental results). Obtaining the deformation profile of the specimen for each mode shape allows us to understand the PDs different behaviors. Finite element models were built using SOLID45 hexagonal mesh elements. The PD cavity volumes were approximated as empty regions; however, the mass of unfused powder was modeled using a MASS21 nodal mass element and was tied to external nodes of cavity walls using RBE3 elements to prevent adding stiffness to the model [35].

Table 2 Chemical composition of Inconel 718 powder according to Praxair's data [34]

Element	Composition range (%)
Ni	50.000–55.000
Cr	17.000–21.000
Fe	15.000–21.000
Nb+Ta	4.750–5.500
Mo	2.800–3.200
Ti	0.650–1.150
Al	0.200–0.800
Co	≤1.000
Mn	≤0.350
Si	≤0.350
Cu	≤0.300
C	≤0.080
Ta	≤0.050
P	≤0.015
S	≤0.015
B	≤0.006

In the modal analysis, the boundary conditions were unconstrained on all sides, and the first two modes (bending and torsional modes) were investigated. The mode shapes of the fully fused model are shown in Fig. 4. The mode shapes of all the specimens are similar, except for minor differences, including frequency shifts (on average, a 4.1% shift for the first mode and a 3.3% shift for the second mode, according to test results) and deflection differences due to internal cavity location and damper effects (due to the stiffness and mass variations resulting from the PDs).

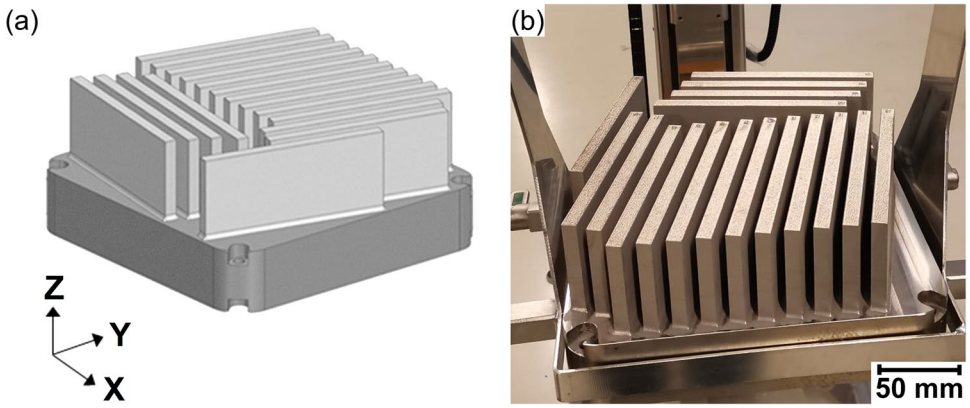

Fig. 3 **a** Isometric view of CAD model and **b** printed specimens on the build plate

Table 3 Dimensions of PDs, volume fraction of PDs, and mass of PD-integrated specimens

Specimen no.	Centerline-based cavity dimensions (mm)	Number of cavities	Mass (g)	Volume fraction (%)	Cavity locations
0 (fully fused)	-	-	731	-	-
1	80 × 40 × 6	1	670	20	Center
2	80 × 40 × 6	1	669	20	Tip
3	40 × 40 × 6	1	697	10	Center
4	40 × 40 × 6	1	701	10	Tip
5	20 × 40 × 6	1	711	5	Center
6	20 × 40 × 6	1	712	5	Tip
7	40 × 40 × 6	2	670	20	Center
8	40 × 40 × 6	2	669	20	2 Tips
9	40 × 40 × 6	2	671	20	Tip
10	20 × 40 × 6	2	700	10	Center
11	20 × 40 × 6	2	698	10	2 Tips
12	20 × 40 × 6	2	701	10	Tip
13	20 × 40 × 6	3	685	15	Center
14	20 × 40 × 6	3	684	15	Center and 2 tips
15	20 × 40 × 6	3	685	15	Tip
16	20 × 40 × 6	4	669	20	Center

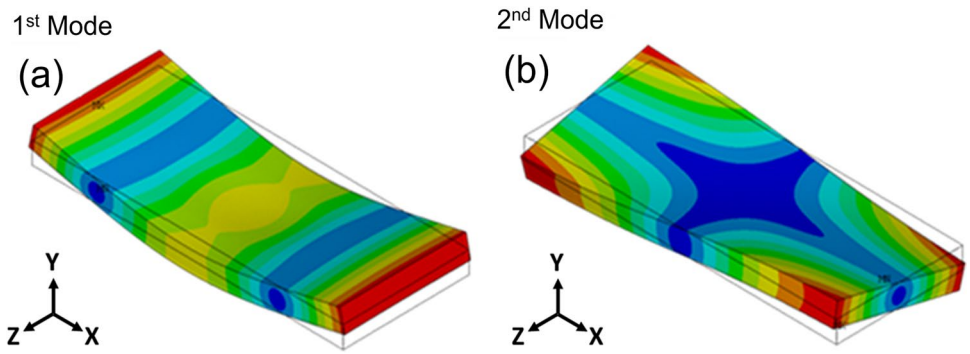

Fig. 4 The first two mode shapes (bending and torsional modes) of the fully fused model

The purpose was to determine the effectiveness of particle damper positions using these mode shapes. In this regard, significant progress has been made, and the mode shapes derived from the analysis have played a crucial role in interpreting the damping performance.

2.4 Experimental setup and test plan for extracting damping ratio

The experimental setup used to determine the damping ratio of the specimens is presented in Fig. 5a. The modal tests were performed on unconstrained specimens (i.e., free-free boundary condition). To achieve the free-free boundary condition, a soft foam (sponge) was used, and the contact area between the soft foam and test sample was minimized (approximately 5% of the total surface area of the specimen) to prevent damping from the ground. The excitation was applied using an impact hammer (Dytran Dynapulse 5800B4), and the corresponding response of the system was measured using an accelerometer (Dytran 3225F1). To collect the impact and response data, a National Instruments NI USB-4431 dynamic signal acquisition module was used, with a frequency resolution and sampling rate of 0.5 Hz and 102,400 Hz, respectively.

Twelve points were identified for excitation (hammer impact), as shown in Fig. 5b. An accelerometer was placed at the center of the bottom surface of the specimens. In each test, five impacts were applied to each point to calculate the FRFs. Furthermore, the results obtained from these twelve points were averaged. Using the impact and response data, the FRFs were plotted over a frequency range of 0–4000 Hz to include the first two natural frequencies of the specimens.

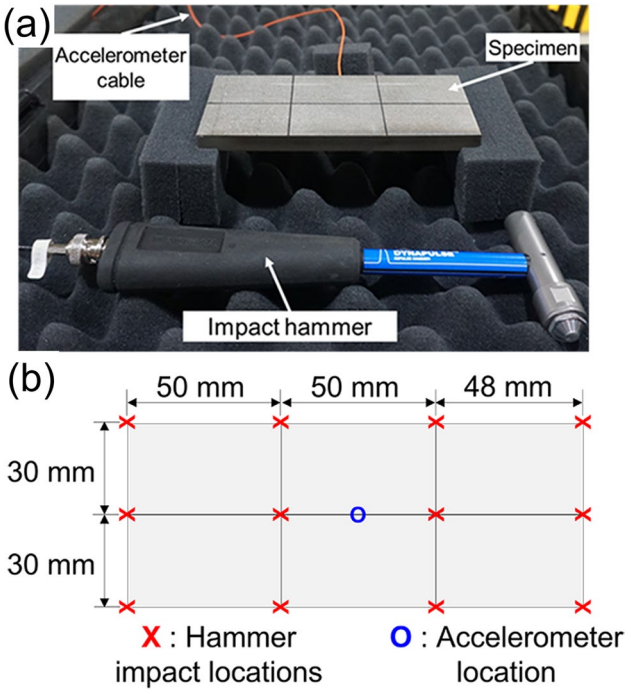

Fig. 5 **a** Hammer impact experimental test setup. **b** Schematic of hammer impact and accelerometer locations

2.5 Methods of analysis

In the first step of data analysis, the rational fraction polynomial (RFP) method, which uses a complex function and user-defined frequency values [36], was used to fit a curve on the test data for each FRF measurement, obtain the corresponding natural frequencies, and calculate the damping ratios.

In the second step, the RSS of the overall acceleration function was calculated up to 4000 Hz to quantify the average vibration amplitude of the specimens. For this purpose, acceleration data were collected from various points on the beams, and the dynamic behavior was evaluated using the following equations:

$$A(\omega) = \sum_{i=1}^{N} a_i(\omega) \tag{1}$$

$$RSS = \sqrt{\sum_{i=0}^{4000} A\left(\omega_i\right)^2} \tag{2}$$

where N is the number of measured values, ω is the frequency, a is the acceleration measured from the accelerometer at a specific natural frequency, and A is the sum of measured a values.

3 Results and discussion

3.1 Determination of particle mass and packing density

The volume of the fully fused beam was 88.8 cm^3, and its mass was 731 g, giving a density of 8.23 g/cm^3 (compared to 8.2 g/cm^3 according to the datasheet from Praxair). The average powder bed density (5.0 g/cm^3 according to the datasheet of Praxair) at the cavity locations was calculated as 4.511 g/cm^3 (~55% relative density). These values indicate that body-integrated cavity increments reduce the mass of the specimen (listed in Table 3) compared with the fully fused structure.

3.2 Results of tests and analysis

From the measured FRFs, the modal parameters (natural frequencies and damping ratios) for the first two modes were determined using the RFP method and investigated based on the test matrix given in Table 3. An example FRF

measurement and the corresponding coherence plot is given in Fig. 6. It is evident that, excluding the antiresonance regions, where the actual response remains minimal, rendering the output-input relation indistinct, the coherence values remain close to unity across the frequency range of 0–4000 Hz. Consequently, given the coherence values consistently exceeding 90% around the resonant peaks, their reliability in extracting the modal parameters is considered satisfactory.

For the fully fused specimen, the natural frequencies of the first and second modes were 2197 Hz and 3424 Hz, and their damping ratios were 7.1×10^{-4} and 5.0×10^{-4}, respectively. These values were used for comparison to identify the changes in the damping performance of the specimens with integrated PDs. These comparisons are visualized in Figs. 8, 9, and 10 and described below in detail.

As mentioned in the Section 2.3, the first two natural frequencies and the corresponding (bending and torsional) mode shapes were also obtained from FEA. Due to the approximations applied in the numerical modeling, slight differences in the natural frequencies were observed. For example, the modeling outputs for the first two natural frequencies for the fully fused specimen were 2331 Hz and 3339 Hz; these values differed by 6.1% and 2.5% compared with the experimentally obtained values, respectively. The experimental results for all the specimens with PDs are provided in Table 4 along with the RSS values of the measured FRFs. These results show that the PDs reduced the displacement amplitudes, and thus, the RSS values decreased around the natural frequency regions. However, over the entire frequency range up to 4000 Hz, the RSS values may increase

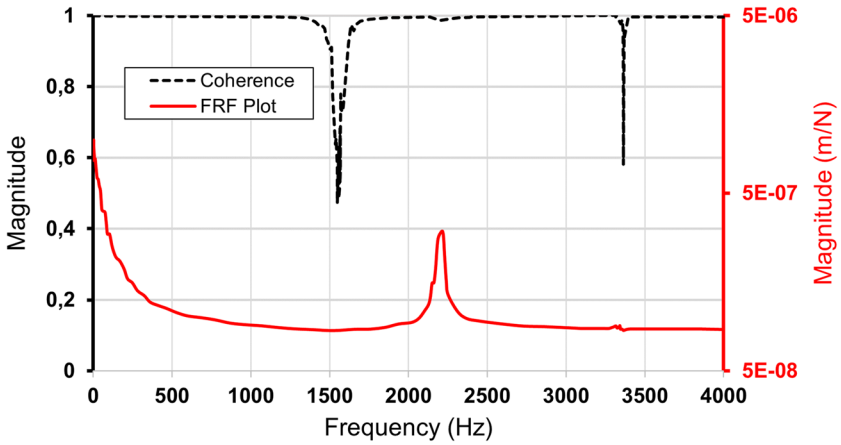

Fig. 6 Calculated FRF and the corresponding coherence plot for specimen 1

Table 4 Experimentally determined modal parameters of the specimens and the RSS values of the calculated FRFs

Parameter	1st mode		2nd mode		RSS
	Frequency (Hz)	Damping ratio	Frequency (Hz)	Damping ratio	Experiment (0–4000 Hz)
0 (fully fused)	2197	7.1e-4	3424	5.0e-4	0.036
1	2201	7.7e-3	3340	3.1e-3	0.060
2	2207	6.4e-3	3294	4.7e-3	0.039
3	2238	5.3e-3	3321	7.7e-4	0.034
4	2168	3.1e-3	3424	2.0e-3	0.043
5	2204	3.3e-3	3373	5.2e-4	0.032
6	2218	2.4e-3	3437	1.3e-3	0.033
7	2139	5.8e-3	3317	2.3e-3	0.051
8	2111	4.7e-3	3396	3.0e-3	0.051
9	2202	7.1e-3	3339	2.4e-3	0.045
10	2186	4.7e-3	3342	8.4e-4	0.035
11	2196	2.6e-3	3432	1.8e-3	0.032
12	2175	2.9e-3	3453	1.5e-3	0.038
13	2149	4.3e-3	3337	1.8e-3	0.037
14	2178	4.3e-3	3436	3.2e-3	0.029
15	2203	4.8e-3	3373	1.7e-3	0.038
16	2145	4.6e-3	3376	3.8e-3	0.038

in the other regions of the measured FRFs since the stiffness of the specimens also decreases with PDs. This phenomenon is illustrated in Fig. 7, which shows the measured FRFs of the fully fused specimen and the specimen with the lowest RSS ratio, specimen 14.

The highest damping ratios for the first and second modes were observed for specimen 1 as 7.7×10^{-3} (see Fig. 8a) and specimen 2 as 4.7×10^{-3} (see Fig. 8c). Compared with the fully fused specimen, the damping ratios using PDs increased by factors of up to 10.8 for the first mode and 9.4 for the second mode (as given in Table 4).

The results showed that the damping performance of PDs depends on the volume fraction, location, number, and length of PDs. As can be seen in Fig. 8, the damping ratios increased as the volume fraction increased. An overall improvement in damping ratio for both the first and the second modes based on the location of the PDs for the same volume fraction was observed, as presented in Fig. 9. Specifically, specimens with PDs located closer to the center of the main body resulted in a higher damping ratio for the first mode compared with PDs located around the tip region. In contrast, for the second mode, the location effect is the opposite (i.e., PDs closer to the tip region exhibit better damping for the second mode). Detailed discussions of these results in terms of the effects of each studied parameter are provided in the following sections.

The highest damping ratios for the first and second modes were observed for specimen 1 as 7.7×10^{-3} (see

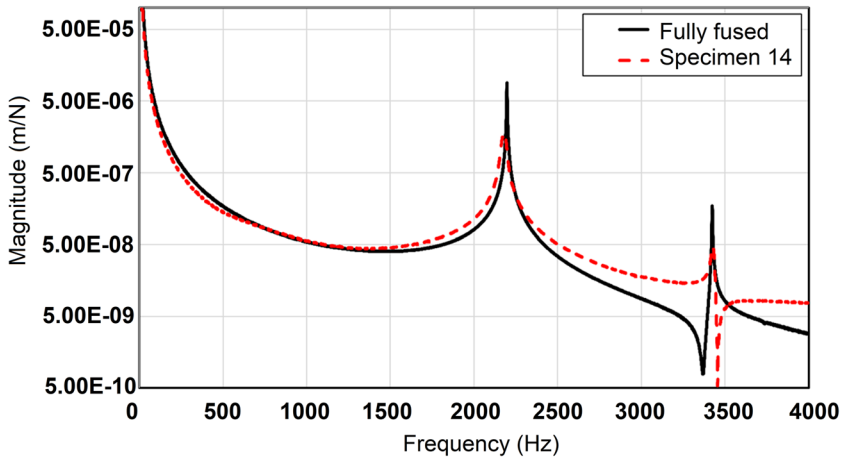

Fig. 7 FRF comparison of fully fused beam and specimen 14

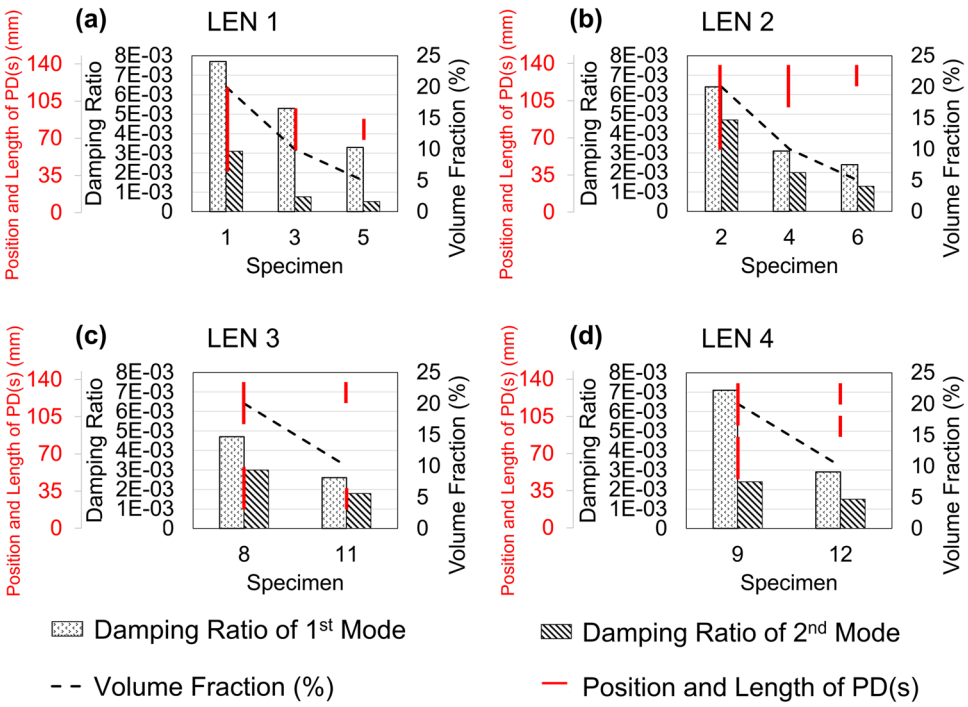

Fig. 8 Effect of length of particle dampers **a** LEN 1, **b** LEN 2, **c** LEN 3, and **d** LEN 4. Red lines represent the cavity length and location for illustration purposes to compare the data clearly

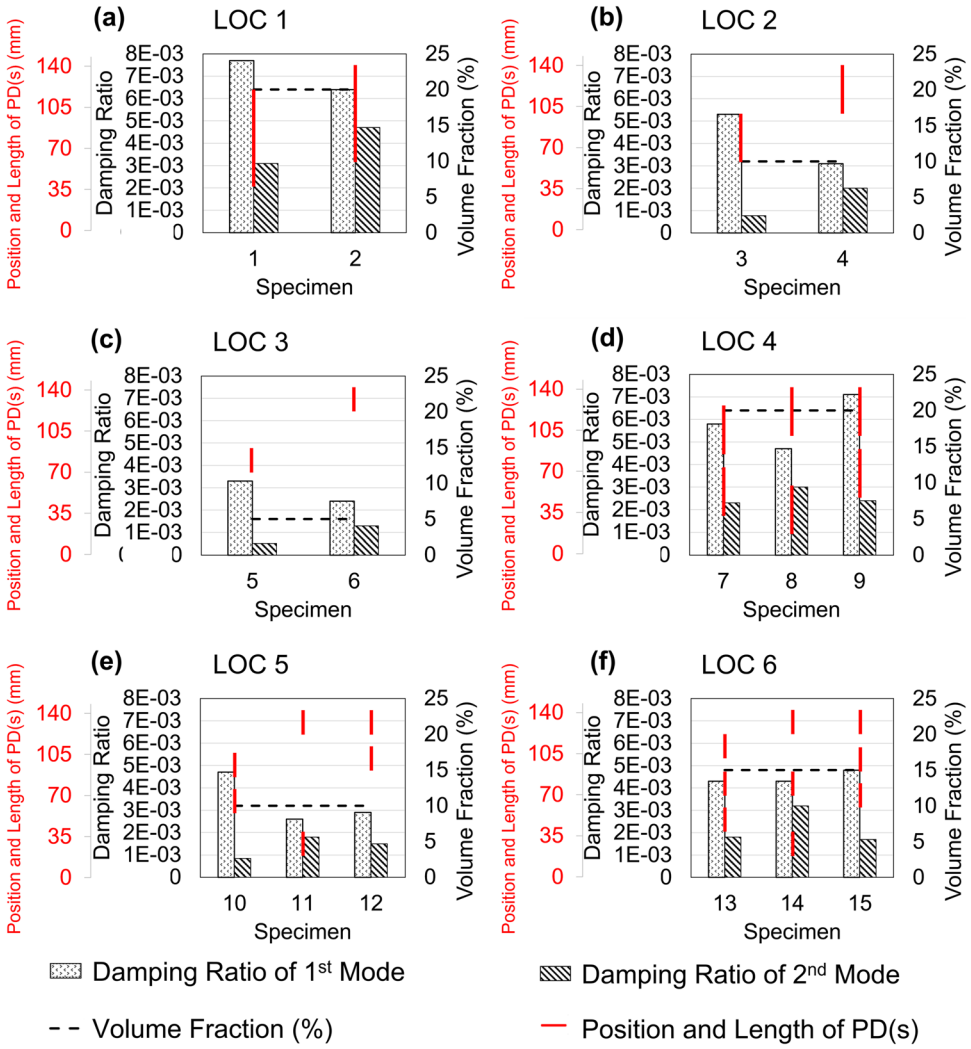

Fig. 9 Effect of the dampers on different mode shapes **a** LOC 1, **b** LOC 2, **c** LOC 3, **d** LOC 4, **e** LOC 5, and **f** LOC 6. Red lines represent the cavity length and location for illustration purposes to compare the data clearly

Fig. 8a) and specimen 2 as 4.7×10^{-3} (see Fig. 8c). Compared with the fully fused specimen, the damping ratios using PDs increased by factors of up to 10.8 for the first mode and 9.4 for the second mode (as given in Table 4).

The results showed that the damping performance of PDs depends on the volume fraction, location, number, and length of PDs. As can be seen in Fig. 8, the damping ratios increased as the volume fraction increased. An overall improvement in damping ratio for both the first and the second modes based on the location of the PDs for the same volume fraction was observed, as presented in Fig. 9. Specifically, specimens with PDs located closer to the center of the main body resulted in a higher damping ratio for the first mode compared with PDs located around the tip region. In contrast, for the second mode, the location effect is the opposite (i.e., PDs closer to the tip region exhibit better damping for the second mode). Detailed discussions of these results in terms of the effects of each studied parameter are provided in the following sections.

3.2.1 Size effect of the unfused cavities

The size effect of the PDs was investigated using the LEN 1–4 groups. The damping ratios for the first two modes of all specimens are shown in Fig. 8. The calculated damping ratios for specimens 1, 2, 8, and 9 were the highest in their groups because these PDs have the highest volume fractions. This indicates that, as volume fractions decrease, the damping performance also deteriorates for the first two modes. The reduction rate (as a function of volume fraction) in the damping ratios depends on the locations of the PDs, primarily due to their mode shape profiles. If the length of the PDs increases, so does its likelihood to coincide with the maximum deformation region of the modes, thereby increasing the effectiveness of the damping performance to an extent determined by the alignment with the mode shape profile. For example, in Fig. 8a, three specimens each have a single PD, but with different lengths around the central region, and the damping performance for the first mode significantly

decreases as the PD length decreases. However, no significant difference is observed for the damping ratio of the second mode for specimens 3 and 5 because the PDs are shorter and farther from the maximum displacement location of the second mode. Similar trends are also observed in groups LEN 2–4, as shown in Fig. 8b–d.

3.2.2 Location effect of the unfused cavities

The LOC 1–6 groups were used to evaluate the effect of the PD location, with the result shown in Fig. 9. The results indicate that, for the first mode, PDs located closer to the center region of the beams are more effective, whereas PDs placed closer to the tip are more effective for the second mode. As discussed in Section 3.2.1, this can be explained using the deformation profile of the mode shapes. From Fig. 4, the displacement of the middle section of the specimen is higher for the first bending mode, whereas the displacement of the tip is higher for the second mode. Thus, PDs located at the tips increase the damping for the second mode, as shown in Fig. 9a–c for LOC 1–3.

For specimens with multiple PDs (LOC 4–6 groups), the results are presented in Fig. 9d–f. The specimens in LOC 4 and LOC 5 have two PDs, and the specimens in LOC 6 have 3 PDs along the length of the beams. Similar to the results obtained for beams with a single PD, the location of the PDs is the most critical factor for improving the damping of a specific mode. For example, in the LOC 4 group, specimen 8 has PDs located at both tips; thus, the damping ratio of the second mode is the highest for this group, with a value of 3.0×10^{-3}. However, specimen 9 has the best damping performance for the first mode since one of the PD locations is closely aligned with the high deformation zone of the first mode. Although both PDs of specimen 7 are located near the center, their damping performance is similar to that of specimen 9 since there is a gap between the two PDs which aligns with the location of maximum displacement for the first mode. For LOC 5, despite the locations of the PDs being similar to those in LOC 4, the order of decreasing damping performance for the specimens is 10, 12, and 11, as opposed to the order of 12, 10, and 11 for the first mode. The reason for this difference is that the PD lengths are shorter than in LOC 4 and they are not located in the high deformation zones of the first mode shape as they are in LOC 4. The PDs in specimen 10 are located closer to the center than they are for the other specimens; thus, it has the highest damping ratio. Finally, the specimens in LOC 6 also show that PDs located at the center are more effective in damping the first mode, while those placed at the tips are more effective in damping the second mode. From the results of LOC 4–6, it can be concluded that distributing the locations of PDs over the main body generally leads to increased damping ratios for both modes.

3.2.3 Number effect of the unfused cavities

Figure 10 shows the results for specimens in the NOD 1–4 groups. Among the specimens in NOD 1 (see Fig. 10a),

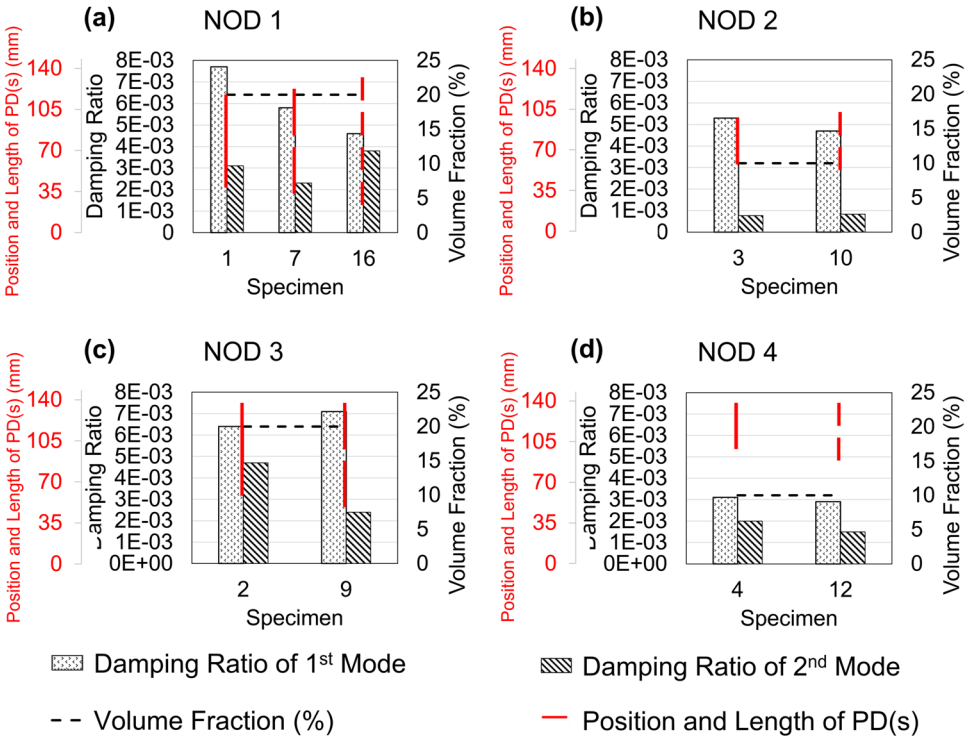

Fig. 10 Effect of the number of dampers **a** NOD 1, **b** NOD 2, **c** NOD 3, and **d** NOD 4. Red lines represent the cavity length and location for illustration purposes to compare the data clearly

specimen 1, which has a single cavity for the same volume fraction, is the most effective for damping the first mode. However, specimen 16 shows the best damping performance for the second mode in this group due to the mode shape deformation profile. Furthermore, the damping ratio of the first mode for specimen 7 is between that of specimens 1 and 16; however, its damping performance is the lowest for the second mode. For this specimen, although the PDs are closer to the tips than they are for specimen 1, their locations are also closer to the nodal points for the second mode shape, leading to a lower damping ratio. These results indicate that the location of PDs has a stronger influence on damping performance than the number of PDs. Similarly, for specimens in NOD 2 (see Fig. 10b), specimen 3 with a single cavity was compared with its two-cavity counterpart, specimen 10. The damping ratio of the first mode is higher for specimen 3 because its cavity covers more of the high deformation zone for the first mode, as opposed to specimen 10, which has two distributed cavities that are farther away from the deformation zone. However, the damping ratios of the second mode for both specimens are similar since they both do not extend close to the tips which are the high deformation zones for the second mode. Similar results are observed for the specimens of NOD 4, as shown in Fig. 10d. Based on these results, when cavities are separated, there may not be good alignment with the maximum deflection zone because of the locations of the PDs. For NOD 3, the impact of cavity location was observed more clearly, even with a small shift in location. As a result, the change in the number of PDs did not have a significant effect on damping performance while keeping the volume fractions and locations of the PDs similar. However, the effectiveness of the PDs is strongly correlated with their locations.

4 Conclusion

The dynamic behavior of Inconel 718 samples with integrated PDs produced by L-PBF was investigated in this study. Modal tests were performed, and the modal parameters were determined from the measured FRFs up to 4000 Hz using the RFP method. In the measured frequency range, two modes (bending and torsional modes) were identified. The effects of several parameters, including the number of PDs, location, and size, on the damping characteristics of the fabricated beams were examined through the application of a DoE analysis. Based on the results, three valuable conclusions can be drawn: (1) Damping performance improves with higher PD volume fractions, (2) the damping performance of a particular mode is most significantly affected by the PD location due to mode shape deformation profiles, and (3) damping ratios are enhanced by up to a factor of 10 compared to those of a fully fused specimen.

In summary, although integrating PDs into a structure by AM offers the potential for lighter, custom, and optimized designs with better damping performance, more detailed studies are necessary. For example, to better understand how PDs affect dynamic behavior and enable the intelligent design of structures integrated with PDs, high-fidelity numerical models should be developed. In addition, designing a larger DoE and experimentally determining the damping characters (for higher modes and different boundary conditions) may enable further optimization and novel applications.

Furthermore, research has brought to light that utilizing the design flexibility offered by AM facilitates the fabrication of more effective PD designs compared to conventional methods. This emphasizes the appeal of AM for parts with complex/intricate geometries and underscores its potential for advancing PD applications across diverse domains. The illustrated indirect impact of AM on elevating system performance reaffirms its pivotal role in propelling technological advancement.

Funding Open access funding provided by the Scientific and Technological Research Council of Türkiye (TÜBİTAK).

Declarations

This study was carried out under the TUBITAK Technology and Innovation Support Program (Grant number: 5158001).
The authors have no relevant financial or non-financial interests to disclose.
All authors contributed to the interpretation of the results. The design of experiments was contributed by all authors. Conducting experiments, data collection, and analysis were performed by Birol Ozcevik. Data analysis and interpretation were also led by Bekir Bediz and Emrecan Soylemez. The first draft was written by Birol Ozcevik. Then, multiple revisions were done by Bekir Bediz and Emrecan Soylemez. All authors read and approved the final manuscript.

References

1. Zhang C, Chen T, Wang X, Yu K (2016) Influence of cavity on the performance of particle damper under centrifugal loads. J Vib Control 22:1704–1714. https://doi.org/10.1177/1077546314544351
2. Lu Z, Wang Z, Masri SF, Lu X (2018) Particle impact dampers: past, present, and future. Struct Control Health Monit 25(1):e2058. https://doi.org/10.1002/stc.2058

3. Simonian SS (1995) Particle beam damper. Smart Structures and Materials: Passive Damping 2445:149–160. https://doi.org/10.1117/12.208884
4. Mao K, Wang MY, Xu ZZ, Chen T (2004) Simulation and characterization of particle damping in transient vibrations. J Vib Acoust Trans ASME 126:202–211. https://doi.org/10.1115/1.1687401
5. Saeki M (2005) Analytical study of multi-particle damping. J Sound Vib 281:1133–1144. https://doi.org/10.1016/j.jsv.2004.02.034
6. Fowler BL, Flint EM, Olson SE (2001) Design methodology for particle damping. Smart Structures and Materials: Damping and Isolation 4331:186–197. https://doi.org/10.1117/12.432703
7. Xiao W, Li J, Wang S, Fang X (2016) Study on vibration suppression based on particle damping in centrifugal field of gear transmission. J Sound Vib 366:62–80. https://doi.org/10.1016/j.jsv.2015.12.014
8. Olson SE (2003) An analytical particle damping model. J Sound Vib 264:1155–1166. https://doi.org/10.1016/S0022-460X(02)01388-3
9. Ehlers T, Tatzko S, Wallaschek J, Lachmayer R (2021) Design of particle dampers for additive manufacturing. Addit Manuf 38:101752. https://doi.org/10.1016/j.addma.2020.101752
10. Papalou A, Masri SF (1996) Performance of particle dampers under random excitation. J Vib Acoust 118:614–621. https://doi.org/10.1115/1.2888343
11. Panossian HV (1992) Structural damping enhancement via non-obstructive particle damping technique. J Vib Acoust 114:101–105. https://doi.org/10.1115/1.2930221
12. Friend RD, Kinra VK (2000) Particle impact damping. J Sound Vib 233:93–118. https://doi.org/10.1006/jsvi.1999.2795
13. Fowler BL, Flint EM, Olson SE (2000) Effectiveness and predictability of particle damping. Smart Struct Mater 3989:356–367. https://doi.org/10.1117/12.384576
14. Sánchez M, Carlevaro CM, Pugnaloni LA (2014) Effect of particle shape and fragmentation on the response of particle dampers. JVC/J Vib Control 20:1846–1854. https://doi.org/10.1177/1077546313480544
15. Huang SH, Liu P, Mokasdar A, Hou L (2013) Additive manufacturing and its societal impact: a literature review. Int J Adv Manuf Technol 67:1191–1203. https://doi.org/10.1007/s00170-012-4558-5
16. Pereira T, Kennedy JV, Potgieter J (2019) A comparison of traditional manufacturing vs additive manufacturing, the best method for the job. Procedia Manuf 30:11–18. https://doi.org/10.1016/j.promfg.2019.02.003
17. Scott-Emuakpor O, George T, Runyon B et al (2018) Investigating damping performance of laser powder bed fused components with unique internal structures. Am Soc Mech Eng Turbo Expo 7C. https://doi.org/10.1115/GT2018-75977
18. Ehlers T, Lachmayer R, Vajna S, Halle T (2020) Integrated design engineering, 1st ed. Springer International Publishing, Cham, pp 287–323. https://doi.org/10.1007/978-3-030-19357-7_9
19. Ehlers T, Lachmayer R (2021) Design of a motorcycle triple clamp optimised for stiffness and damping. In: Proceedings of the Munich symposium on lightweight design. Springer Vieweg, Berlin, Heidelberg, pp 1–17. https://doi.org/10.1007/978-3-662-63143-0_1
20. Ganter NV, Ehlers T, Gembarski PC, Lachmayer R (2021) Additive refurbishment of a vibration-loaded structural component. In: Proceedings of the design society. Cambridge University Press, pp 345–354. https://doi.org/10.1017/pds.2021.35
21. Pourtavakoli H, Parteli EJR, Pöschel T (2016) Granular dampers: does particle shape matter? New J Phys 18:1–11. https://doi.org/10.1088/1367-2630/18/7/073049
22. Guo H, Ichikawa K, Sakai H et al (2022) Numerical and experimental analysis of additively manufactured particle dampers at low frequencies. Powder Technol 396:696–709. https://doi.org/10.1016/j.powtec.2021.11.029
23. Harduf Y, Setter E, Feldman M, Bucher I (2023) Modeling additively-manufactured particle dampers as a 2DOF frictional system. Mech Syst Signal Process 187:109928. https://doi.org/10.1016/j.ymssp.2022.109928
24. Ehlers T, Lachmayer R (2022) Design of particle dampers for laser powder bed fusion. Appl Sci 12:1–26. https://doi.org/10.3390/app12042237
25. Scott-Emuakpor O, George T, Runyon B et al (2019) Forced-response verification of the inherent damping in additive manufactured specimens. Mech Addit Adv Manuf 8:81–86. https://doi.org/10.1007/978-3-319-95083-9_15
26. Scott-Emuakpor O, Beck J, Runyon B, George T (2021) Determining unfused powder threshold for optimal inherent damping with additive manufacturing. Addit Manuf 38:1–9. https://doi.org/10.1016/j.addma.2020.101739
27. Scott-Emuakpor O, George T, Runyon B et al (2019) Sustainability study of inherent damping in additively manufactured nickel alloy. AIAA J 57:456–461. https://doi.org/10.2514/1.J057608
28. Scott-Emuakpor O, George T, Runyon B et al (2020) Assessing additive manufacturing repeatability of inherently damped nickel alloy components. J Eng Gas Turbine Power 142:1–8. https://doi.org/10.1115/1.4044314
29. Goldin A, Scott-Emuakpor O, George T et al (2021) Structural dynamic and inherent damping characterization of additively manufactured airfoil components. J Eng Gas Turbine Power 143:051022-1–051022-8. https://doi.org/10.1115/1.4050022
30. Qi H, Azer M, Ritter A (2009) Studies of standard heat treatment effects on microstructure and mechanical properties of laser net shape manufactured INCONEL 718. Metall Mater Trans A 40:2410–2422. https://doi.org/10.1007/s11661-009-9949-3
31. Ding RG, Huang ZW, Li HY et al (2015) Electron microscopy study of direct laser deposited IN718. Mater Charact 106:324–337. https://doi.org/10.1016/j.matchar.2015.06.017
32. Hosseini E, Popovich VA (2019) A review of mechanical properties of additively manufactured Inconel 718. Addit Manuf 30:100877. https://doi.org/10.1016/j.addma.2019.100877
33. Chang S-H (2009) In situ TEM observation of γ', γ'' and δ precipitations on Inconel 718 superalloy through HIP treatment. J Alloys Compd 486:716–721. https://doi.org/10.1016/j.jallcom.2009.07.046
34. Praxair S.T. Technology Inc (2018) TruFormTM metal powders for additive manufacturing - TruFormTM 718 Metal Powder. Indianapolis, IN, USA. Available online: https://www.i3dmfg.com/wp-content/uploads/2019/01/TruForm-718-Metal-Powders.pdf. Accessed 16 Sept 2023
35. Rahman MM, Bakar RA, Noor MM et al (2008) Fatigue life prediction of spot-welded structures: a finite element analysis approach. Eur J Sci Res 22:444–456
36. Richardson MH, Formenti DL (1982) Parameter estimation from frequency response measurements using rational fraction polynomials. IMAC Conference 1:1–15